



## Segmentation of interwoven 3d tubular tree structures utilizing shape priors and graph cuts

Christian Bauer<sup>a,\*</sup>, Thomas Pock<sup>a</sup>, Erich Sorantin<sup>b</sup>, Horst Bischof<sup>a</sup>, Reinhard Beichel<sup>c,d</sup>

<sup>a</sup> Institute for Computer Graphics and Vision, Graz University of Technology, Inffeldgasse 16, A-8010 Graz, Austria

<sup>b</sup> Department of Radiology, Medical University Graz, Auenbruggerplatz 9, A-8010 Graz, Austria

<sup>c</sup> Department of Electrical and Computer Engineering, The University of Iowa, Iowa City, IA 52242, USA

<sup>d</sup> Department of Internal Medicine, The University of Iowa, Iowa City, IA 52242, USA

### ARTICLE INFO

#### Article history:

Received 13 August 2008

Received in revised form 6 October 2009

Accepted 10 November 2009

Available online 22 November 2009

#### Keywords:

Tubular structure segmentation

Vessel tree separation

Liver vessel segmentation

### ABSTRACT

The segmentation of tubular tree structures like vessel systems in volumetric datasets is of vital interest for many medical applications. We present a novel approach that allows to simultaneously separate and segment multiple interwoven tubular tree structures. The algorithm consists of two main processing steps. First, the tree structures are identified and corresponding shape priors are generated by using a bottom-up identification of tubular objects combined with a top-down grouping of these objects into complete tree structures. The grouping step allows us to separate interwoven trees and to handle local disturbances. Second, the generated shape priors are utilized for the intrinsic segmentation of the different tubular systems to avoid leakage or undersegmentation in locally disturbed regions. We have evaluated our method on phantom and different clinical CT datasets and demonstrated its ability to correctly obtain/separate different tree structures, accurately determine the surface of tubular tree structures, and robustly handle noise, disturbances (e.g., tumors), and deviations from cylindrical tube shapes like for example aneurysms.

© 2009 Elsevier B.V. All rights reserved.

### 1. Introduction

Blood vessels and airways of the human body form dense tubular tree-like structures. Analysis of their morphology (structure, diameters, branching patterns, etc.) is of vital interest for many clinical applications and facilitates diagnosis, quantification and monitoring of disease, preoperative planning, or intraoperative navigation. Modern medical imaging modalities depict tubular systems of the human body in great detail. However, the manual analysis and quantification of these structures is impracticable in clinical routine due to their complexity. Therefore, automated and robust segmentation methods for tubular tree structures are needed. For example, planning of liver surgery requires the segmentation and analysis of portal and hepatic veins shown in Fig. 1 (see Reitinger et al., 2006 for details). In this context, a segmentation method has to address several issues to be clinically applicable (Fig. 1):

- Deliver correct 3d reconstructions of all vessel trees in a volume of interest (we assume that vessel trees should be free of loops).

- Provide an automated separation of the different interwoven vessel systems (e.g. portal and hepatic veins) that may have the same gray-values and can appear to be overlapping in image data due to partial volume effects.
- Have the ability to segment thin vessels with low contrast. This is necessary for an accurate determination of the volume of liver segments (Selle et al., 2002).
- Differentiate vessels from other adjacent structures with the same gray-values such as tumors.
- Handle cases where parts of the tubular tree structure are locally disturbed; e.g. due to imaging artifacts or disease.
- Require only minimal user interaction.

Similar requirements to that outlined above can be found in many other application domains (e.g., segmentation of lung vasculature).

In the literature, many publications dealing with the segmentation of tubular tree-like structures can be found. For a survey we refer to the work of Kirbas and Quek (2003), and a discussion of recent approaches can be found in Lee et al. (2007) or Li and Yezzi (2007), for example. To our knowledge, the so far proposed methods only partially address the before mentioned issues. In the next paragraphs we will briefly discuss conventional approaches to motivate our approach, while other more closely to our work related publications are discussed in Sections 2 and 5.2.

\* Corresponding author. Tel.: +43 316 873 5031; fax: +43 316 873 5011.  
E-mail address: [cbauer@icg.tugraz.at](mailto:cbauer@icg.tugraz.at) (C. Bauer).

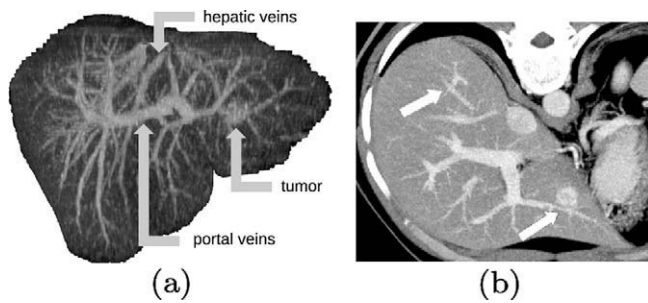


**Fig. 1.** Portal and hepatic vessel trees of a diseased liver. (a) Maximum intensity projection (MIP) showing the vessel trees. (b) Axial CT image showing a tumor in proximity to vessels and overlapping vessel trees (arrows).

Conventional approaches may be roughly grouped into top-down or bottom-up segmentation methods. Top-down segmentation methods segment the targeted structures starting from given seed points by iteratively merging adjacent structures that fulfill a specified segmentation criterion. In contrast, bottom-up segmentation methods do not require such an initialization and evaluate the given segmentation criterion at every voxel of an image. Typical examples for top-down methods are region growing or active contours like snakes or levelsets that require an appropriate initialization such as e.g. (Yi and Ra, 2003; Selle et al., 2002; Lorigo et al., 2001). Typical examples of bottom-up methods are methods based on statistical histogram analysis or methods based on local shape descriptors such as tube detection filters; e.g. (Krissian et al., 2000; Frangi et al., 1998; Soler et al., 2001).

For top-down as well as for bottom-up segmentation methods, local disturbances such as low contrast or partly overlapping image structures with the same gray-value are challenging (e.g. adjacent tumors or multiple partly overlapping vessel trees; see Fig. 1). In case of failure, these methods produce leakage or undersegmentation. In both cases, the segmentation errors that result from such

local disturbances may have a strong influence on the resulting structure of the segmented trees. The separation and segmentation of multiple tubular trees is even more challenging using conventional top-down or bottom-up approaches.

In this paper, we present an approach for the separation and segmentation of interwoven tubular tree structures that addresses the above stated requirements. The main processing steps are illustrated in Fig. 2. To achieve a high robustness against local disturbances, our approach initially identifies and analyzes the structure of the different trees and utilizes this information as a prior for a constrained segmentation step. The utilized shape priors are generated in two steps. Initially, a bottom-up tube detection filter combined with a centerline extraction method is applied. The centerline representation facilitates a high-level analysis of the structural relations between the different tubular objects. Based on this analysis, tree structures are formed in a top-down fashion by utilizing knowledge about the blood or air flow direction in these tube networks. The so obtained information is then utilized as a shape prior for a constrained segmentation and preserves the correct structure/topology of the different trees. This approach allows our method to effectively separate multiple tubular tree structures from one another and to handle local disturbances (e.g., tumors).

The main contribution of our work is a robust method for the simultaneous separation and segmentation of different tubular tree structures including:

- (i) A tube detection filter that is less prone to produce false positive responses compared to other methods known in the literature allowing for a bottom-up identification of tubular objects in complex datasets containing disturbances (Section 5.2.2).
- (ii) An approach for grouping of tubular structures into complete trees that is able to separate multiple interwoven tree structures by utilizing information about the blood flow in vessel systems.

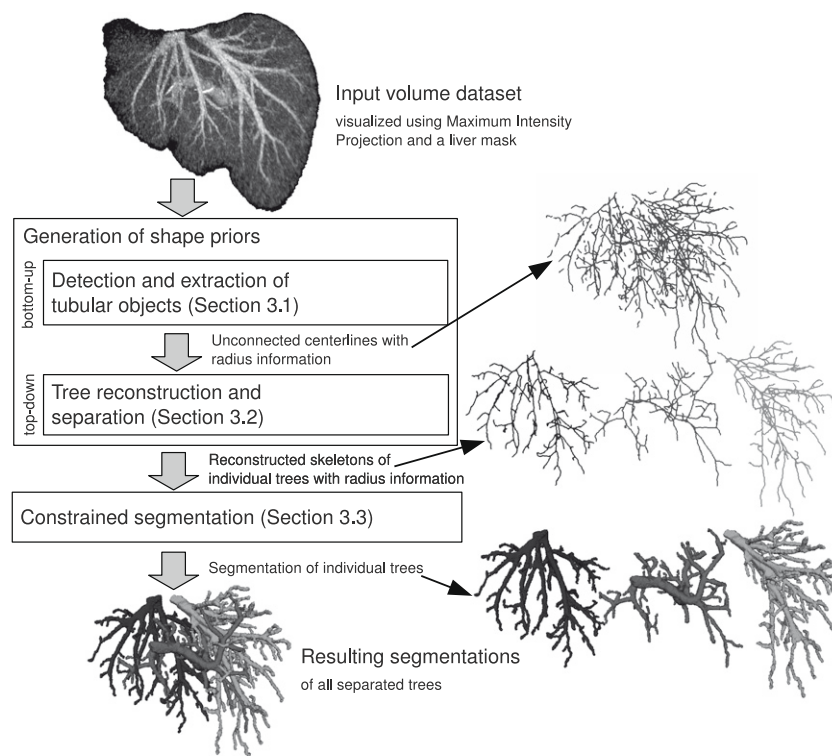


**Fig. 2.** Method overview showing the individual processing steps of the proposed approach and corresponding intermediate results.

- (iii) An intrinsic segmentation method that utilizes structural information about the tubular trees to constrain the actual segmentation, and thus, reduces segmentation errors like leakage or undersegmentation.

We have developed this method for the analysis and segmentation of the vascular trees of the liver. However, we demonstrate the general applicability of our approach on several examples.

## 2. Related work

In this section, approaches more closely related to our approach are discussed as well as preliminary works.

Several methods for the identification/extraction of tubular objects or their centerlines can be found in the literature. Tracking approaches like that of [Aylward and Bullitt \(2002\)](#) or [Wink et al. \(2004\)](#) extract centerlines directly from gray value images but require an appropriate initialization for each single centerline. In contrast, tube detection/enhancement filters like the approaches of [Sato et al. \(1998\)](#), [Krissian et al. \(2000\)](#), or [Frangi et al. \(1998\)](#), do not require such an initialization, because they perform a shape analysis for every pixel in the image resulting in a kind of medialness measure or vessel likelihood. To generate centerline representations from tube detection filter responses, a combination of hysteresis thresholding and local directional non-maximum suppression was used by [Krissian et al. \(2003\)](#) while [Steger \(1998\)](#) utilized an efficient ridge tracking approach for processing 2d images.

For grouping sets of unconnected tubular objects into completely connected networks, only a few methods can be found in the literature like ([Bullitt et al., 2001](#); [Szymczak et al., 2006](#); [Lee et al., 2007](#); [Risser et al., 2008](#); [Beichel et al., 2004](#); [Pock et al., 2005](#)). For this purpose, rather simple criteria like distance or gray value evidence for example were utilized. Such approaches are typically not suitable to differentiate between different tubular tree structures as those shown in [Fig. 1](#). To our knowledge, no method so far has addressed the simultaneous reconstruction and separation of multiple interwoven tree structures. One exception is the work of [Agam et al. \(2005\)](#). They presented a method that is specially tailored to lung vasculature and imposes constraints that are only valid for this specific application. To separate (falsely) connected tubular tree structures in an existing segmentation, an analysis of skeletons is typically utilized to identify splitting points by utilizing radius information ([Selle et al., 2002](#)) or additionally angle information ([Soler et al., 2001](#)). Such approaches are sensitive to segmentation errors, especially to missing parts or leakage where the topology of the extracted centerlines is incorrect.

Some authors denote a structure that is represented as centerlines with corresponding radius information as segmentation (e.g. [Bullitt et al., 2001](#); [Krissian et al., 2003](#)). However, this information does not represent the actual object surface accurately. To obtain accurate segmentations in case of known structure, deformable models were used by [Frangi et al. \(1999\)](#). Recently, [Dou et al. \(2009\)](#) presented a globally optimal graph based segmentation approach for single tree structures.

**Preliminary works:** Our developed tube detection filter (Section 3.1.1) builds on work of [Krissian et al. \(2000\)](#) and [Xu et al. \(1999\)](#). [Krissian et al. \(2000\)](#) presented a multi-scale tube detection filter that combines an estimation of the tube tangent direction based on the Hessian matrix with an offset medialness function to incorporate boundary information, showing that this results in a higher robustness compared to methods that only utilize the eigenvalues of the Hessian matrix (e.g. [Sato et al., 1998](#); [Frangi et al., 1998](#)). Later, they addressed problems related to the inadequateness of the Hessian matrix for tangent direction estimation away from the tube center by utilizing the structure tensor

and a smoothing of tensor fields ([Krissian et al., 2003](#); [Krissian and Farneback, 2003](#)). They additionally introduced parameterized constraints to reduce responses to surface patches, while the same problem has also been addressed by [Xu et al. \(1999\)](#) for the 2d case by introducing a confidence term for the boundary information. One of the main contributions of [Krissian et al. \(2000\)](#) was to derive the optimal relation between the radius of the tube, the radius of the offset medialness function, and the scale to use for computation of the Hessian matrix and the boundary information, such that under the assumption of a single perfectly circular tubular object with known cross-section profile the response at the center is maximized. For the estimation of the tangent direction it is necessary to use a scale that incorporates the whole structure. However, using this scale for obtaining boundary information is generally larger than necessary what can result in a fusion of smaller structures into structures which may be misinterpreted as tubular objects (false responses). We address this issue by using two different scale spaces and obtaining the boundary information on a smaller scale. Additionally, we introduce an adaptive thresholding scheme to eliminate responses away from the tube center in a computationally efficient way. A comparison to [Krissian's](#) approaches is provided in Section 5.2.2.

## 3. Methodology

As outlined in the introduction, our approach consists of three main processing steps ([Fig. 2](#)). In the next sections, the different parts of our method are described in detail. Note that we assume that tubular structures are brighter than the surrounding background and that the datasets are isotropic. If this is not the case, the gray value range can be inverted and datasets resampled, respectively.

### 3.1. Detection and extraction of tubular objects

The first step of our approach is identification of all tubular objects in the whole dataset. Therefore, a tube detection filter with a consecutive centerline extraction is used.

#### 3.1.1. Tube detection filter

Our approach ([Fig. 2](#)) is based on a selective tube detection filter that avoids responses from non-tubular structures. The individual processing steps are described in detail in the following paragraphs.

**3.1.1.1. Tube tangent direction estimation.** For estimation of the orientation of a tube element, the eigenvalues  $|e_1| \geq |e_2| \geq |e_3|$  and associated eigenvectors  $\mathbf{v}_1$ ,  $\mathbf{v}_2$ , and  $\mathbf{v}_3$  of the Hessian matrix are used. For bright tubular structures  $e_1 < 0$  and  $e_2 < 0$  has to hold. This information is used as a preselection criterion, thus avoiding unnecessary computations at other locations. Then, the vector  $\mathbf{v}_3$  represents the tangent orientation of the tube, while  $\mathbf{v}_1$  and  $\mathbf{v}_2$  span a cross-section plane as illustrated in [Fig. 4\(a\)](#). For a tube with known radius  $r$ , the Hessian matrix is computed most stably if the characteristic width of the Gaussian convolution kernel corresponds to the radius  $r$  of the tube. Hence, we define the Hessian scale space for estimation of the tangent direction as

$$\mathcal{H}(\mathbf{x}) = \sigma_{\mathcal{H}}^2 \begin{bmatrix} \partial^2 I^{(\sigma_{\mathcal{H}})} \\ \partial x_i \partial x_j \end{bmatrix} \quad (1)$$

with  $\sigma_{\mathcal{H}} = r$  where  $I^{(\sigma)} = G_{\sigma} \star I(x)$  corresponds to the original image at scale  $\sigma$ .

**3.1.1.2. Offset medialness.** The offset medialness function measures tube-likeness by evaluating boundary information along a circle

of radius  $r$  in the cross-section plane of the tube given by the eigenvectors of the Hessian matrix (Fig. 4(a)). Using a large scale for computation of the boundary information can result in undesired fusion of nearby image structures what can cause false responses. To address this problem we introduce the use of a second (smaller) scale space to compute the boundary information and define the boundariness scale space

$$\mathbf{B}(\mathbf{x}) = \sigma_{\mathbf{B}} \nabla I^{(\sigma_{\mathbf{B}})}(\mathbf{x}) \quad (2)$$

with  $\sigma_{\mathbf{B}} = r^\eta$  where the parameter  $0.0 \leq \eta \leq 1.0$  describes the relation to the tubes scale. Note, that by setting  $\eta = 1.0$  the same scale would be used for obtaining the boundary information as for obtaining the Hessian matrix similar to Krissian's method while setting  $\eta = 0.0$  would result in no noise suppression at all and the method could not account for deviations from a perfectly circular cross-section (e.g. ellipsoid). An initial offset medialness is given by averaging the boundariness contributions  $b_i = |\mathbf{B}(\mathbf{x} + r\mathbf{v}_{\alpha_i})\mathbf{v}_{\alpha_i}|$ :

$$R_0^+(\mathbf{x}, r) = \frac{1}{N} \sum_{i=0}^{N-1} b_i. \quad (3)$$

where  $N$  is the number of samples and is calculated by  $N = \lfloor 2\pi r + 1 \rfloor$  and  $\alpha_i = (2\pi i)/N$ , respectively. The inner product of the boundariness contributions  $b_i$  measures the contribution of the boundariness information in the radial direction  $\mathbf{v}_{\alpha_i} = \cos(\alpha_i)\mathbf{v}_1 + \sin(\alpha_i)\mathbf{v}_2$ . However, (3) also produces responses for isolated edges and non-tube-like structures of high intensity variation (Figs. 3 and 20). To avoid this and facilitate the detection of circular symmetric structures, a criterion that takes the symmetry property of the object into account is used. Considering the distribution of the values  $b_i$ , symmetric structures have a low variance compared to non-symmetric structures as all the boundariness samples along the circle should be approximately equal. To take this information into account, a symmetry confidence based on the variance of the boundariness samples  $s^2(\mathbf{x}, r) = \frac{1}{N} \sum_{i=0}^{N-1} (b_i - \bar{b})^2$  is used:

$$\mathcal{S}(\mathbf{x}, r) = 1 - \frac{s^2(\mathbf{x}, r)}{\bar{b}^2}. \quad (4)$$

For circular symmetric structures,  $s^2$  is very low compared to  $\bar{b}^2$  and hence,  $\mathcal{S}(\mathbf{x}, r)$  is approximately one. For smaller deviations from a perfectly circular cross-section (e.g., an ellipsoidal cross-section profile)  $s^2$  is still low and  $\mathcal{S}(\mathbf{x}, r)$  decreases only slightly. The larger  $s^2$ , the smaller the value  $\mathcal{S}(\mathbf{x}, r)$ , which results in a reduction in the response to non circular symmetric structures. Thus, the final offset medialness is computed as:

$$R^+(\mathbf{x}, r) = R_0^+(\mathbf{x}, r) \mathcal{S}(\mathbf{x}, r). \quad (5)$$

In Fig. 4(b) the response of the offset medialness  $R^+$  for a tube with a Gaussian cross-section profile is shown. Ideally, the response is maximal at the center of the tube and vanishes with increasing distance from the tube center.

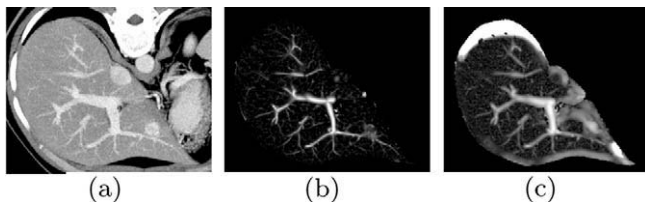


**Fig. 3.** Tube detection filter response inside a liver for a contrast enhanced CT dataset of the liver. (a) Thick slab MIP of axial slices of the original dataset. (b) Response of the proposed tube detection filter. (c) Related approach (Krissian et al., 2000) shows false responses to high gradient edges (e.g. transition to the lung).

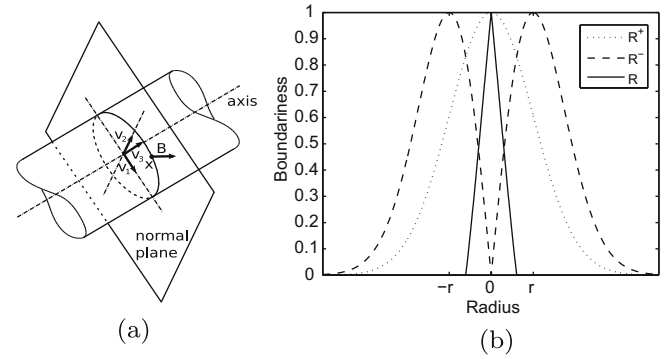


**Fig. 4.** Information used by our tube detection filter. (a) Based on the eigenvectors  $\mathbf{v}_1$ ,  $\mathbf{v}_2$ , and  $\mathbf{v}_3$  of the Hessian matrix the tubes cross-section plane orientation is estimated and gradient information  $\mathbf{B}$  at surface points  $\mathbf{x}$  along a circle in this plane contribute to the offset medialness computation. (b) Combination of medialness measures for a symmetric cross-section of a tubular structure with a Gaussian profile with standard deviation  $r$ .

**3.1.1.3. Center medialness.** To suppress responses near boundaries (away from the tubes center), we propose the use of an adaptive threshold based on gradient information:

$$R^-(\mathbf{x}, r) = \sigma_{\mathcal{H}} |\nabla I^{(\sigma_{\mathcal{H}})}(\mathbf{x})|. \quad (6)$$

Here, the scale  $\sigma_{\mathcal{H}}$  is used such that the information of the whole structure is included. In Fig. 4(b) the response of the offset medialness  $R^-$  for a tube with a Gaussian cross-section profile is shown. Its response is maximal at the surface of the tube element and vanishes at the center.

**3.1.1.4. Combination of medialness responses.**  $R^-(\mathbf{x}, r)$  is used in combination with  $R^+(\mathbf{x}, r)$  as an adaptive threshold that suppresses responses near boundaries (Fig. 4(b)) and avoids artifacts:

$$R(\mathbf{x}, r) = \max\{R^+(\mathbf{x}, r) - R^-(\mathbf{x}, r), 0\}. \quad (7)$$

**3.1.1.5. Computation of the multiscale medialness response.** To take into account the varying sizes of the tubes, the scale-dependent medialness function  $R(\mathbf{x}, r)$  is computed for varying radii for all points  $\mathbf{x}$  of the image domain. The radii are discretized values between  $r_{\min}$  and  $r_{\max}$ , using a linear scale. The multiscale medialness response is obtained by selecting the maximum response over the range of all scales:

$$R_{\text{multi}}(\mathbf{x}) = \max_{r_{\min} \leq r \leq r_{\max}} \{R(\mathbf{x}, r)\}. \quad (8)$$

The scale at which the response is maximal is further used to estimate the radius  $r = \{r_e | R(\mathbf{x}, r_e) = R_{\text{multi}}(\mathbf{x})\}$  and tangent direction  $t = \mathbf{v}_3$  associated with the tube. This information is utilized in subsequent processing steps.

### 3.1.2. Centerline extraction

Based on an analysis of the multiscale medialness response  $R_{\text{multi}}(\mathbf{x})$  of the tube detection filter (Fig. 3(b)), a centerline description for every tube element is extracted (Fig. 2) using a height ridge traversal with hysteresis thresholding. The centerline based description enables the structural analysis of the tube elements which is required for the consecutive reconstruction and separation of biologically reasonable trees (Section 3.2). All centerlines  $\{\mathcal{C}_j\}_{j=1}^m$  consist of an ordered set of centerline points  $\mathcal{C}_j = \{\mathbf{x}_i^j\}_{i=1}^o$ , where  $\mathbf{x}_i^j$  corresponds to the  $i$ th centerline point of the  $j$ th centerline with associated tangent direction  $\mathbf{t}_i^j$  and radius estimate  $r_i^j$ .  $m$  denotes the number of centerlines and  $o$  the number of centerline points of the  $j$ th centerline segment. After extraction of the centerlines, the tube elements are analyzed and postprocessed.



**3.1.2.1. Height ridge traversal.** For height ridge traversal, all local maxima in the medialness map with a value above a threshold  $t_{high}$  are extracted and treated as candidate starting points that are processed in descending order of their associated medialness value. Starting from a candidate point  $\mathbf{x}_0$  with associated positive tangent direction  $\mathbf{t}_0$  and negative tangent direction  $-\mathbf{t}_0$ , the height ridge is traversed independently in both directions. For a current centerline point  $\mathbf{x}_i$  with known tangent direction  $\mathbf{t}_i$ , all local neighbors  $\mathbf{x}_i^n$  with  $\mathbf{x}_i \cdot \mathbf{x}_i^n \cdot \mathbf{t}_i > 0$  are considered, and the neighbor point with the highest medialness response is chosen as the next centerline point  $\mathbf{x}_{i+1}$  on the height ridge. The tangent direction  $\mathbf{t}_{i+1}$  of  $\mathbf{x}_{i+1}$  is set to  $\mathbf{t}_{i+1} = \text{sign}(\overrightarrow{\mathbf{x}_i \mathbf{x}_{i+1}} \cdot \mathbf{t}_i) \mathbf{t}_{i+1}$  to maintain the direction during traversal. The procedure is stopped when the medialness response falls below a given threshold  $t_{low}$  or an already processed centerlinepoint is reached. The second stop condition is necessary to avoid that the same height ridge is traversed several times.

**3.1.2.2. Analysis and postprocessing.** The initially extracted tube elements are analyzed and postprocessed. This is necessary to remove short spurious responses that may result from image noise and to guarantee that only endpoints of centerlines have to be considered for the consecutive tree reconstruction. To discard noise responses, tube elements with an accumulated medialness response of all points along the centerline below the confidence threshold  $t_{conf}$  are discarded. To assure that only endpoints of the centerlines have to be considered for the tree reconstruction step, the centerlines are split at local angle maxima above  $90^\circ$ . This is in particular necessary for trifurcations or higher order furcations. Further, to become robust to outliers the radii and tangent directions of the centerline points are reestimated by averaging along the final centerlines over the 5 local neighbors in both directions (the value of 5 was determined heuristically).

The parameters  $t_{high}$ ,  $t_{low}$ , and  $t_{conf}$  have to be adapted only once for a specific application domain and not for each dataset, as our experiments will show (Section 4).

### 3.2. Tree reconstruction and separation

Having identified all potential tubular structures in the volume of interest, the tube elements are grouped into biologically reasonable trees and interwoven tree structures are separated from one another (Fig. 2). For this purpose the tubes centerlines, tangent directions, and radii are utilized. Additionally, gaps in the initial centerline description which separate parts of the trees are closed. As a result, valid skeletons for the individual trees are reconstructed. During this process, high-level structural representations of the whole trees are derived which describe the parent-child relationships between the tube elements.

#### 3.2.1. Structural representation of the trees

The structural representation of the different trees is based on a directed acyclic graph. All trees together form a forest. The nodes in this graph represent branchpoints of the trees and the edges correspond to tube elements connecting these branchpoints. For all tube elements  $l$  the centerline points  $\mathbf{x}_i^l$  with associated tangent direction  $\mathbf{t}_i^l$ , radius  $r_i^l$ , and the flow direction in tube element  $d^l \in \{+1, -1\}$  are known. If the flow direction is from the first centerline point of the tube element to the last, we set  $d^l = +1$ ; otherwise  $d^l = -1$ . In addition, for every tube element the average radius  $r^l$  and gray-value  $\bar{I}^l$  is known.

#### 3.2.2. Reconstruction and separation

Our tree reconstruction and separation approach utilizes characteristics of biological tree structures and therefore incorporates besides gray-value and distance information also radius and

branching angle information. Incorporation of branching angle information is in particular of importance in case of multiple interwoven tree structures where tube elements tangent each other and seem to overlap due to partial volume effects (Fig. 1(b)). Considering an afferent vessel system, the following characteristics can be observed. Starting from a root element, blood flows into a recursively branching vessel tree. The diameters of the vessels decrease and the direction does not change abruptly. Our reconstruction strategy tries to preserve the flow direction in the trees by taking geometrical properties into account. Starting from given root elements of the trees with known flow direction, tube elements are grouped and connected iteratively using a confidence function. This strategy allows to reconstruct and separate the different trees. During this process, the trees are expanded by iteratively merging unconnected tube elements. Therefore, the endpoints of unconnected tube elements  $\mathbf{x}_i^l$  are considered as candidates for connection to one of the centerline points  $\mathbf{x}_k^l$  of the known trees. First, based on geometric properties, possible connections are identified and preferences based on a confidence function are computed. Second, the connection with the highest confidence is determined and verified based on gray value evidence in the image data. Third, the connection with the highest confidence is inserted into the graph and the procedure is repeated as long as the highest connection confidence stays above a threshold  $c_{min}$ . Determination of the set of possible connections and the confidence for a connection are based on above stated flow preservation constraint (Fig. 5) and primarily utilizes the distance  $d = \max(0, |\overrightarrow{\mathbf{x}_k^l \mathbf{x}_i^l}| - r_k^l)$  and the angles  $\alpha^l = \angle(\overrightarrow{\mathbf{x}_k^l \mathbf{x}_i^l}, d^l \mathbf{t}_i^l)$  and  $\alpha^j = \angle(\overrightarrow{\mathbf{x}_k^l \mathbf{x}_i^l}, d^j \mathbf{t}_j^l)$ . The following hard constraints have to be fulfilled to form biological reasonable tree structures, and therefore, to determine the set of possible connections:

- (i) There must not be sharp turns in the flow direction:  $\alpha^j \leq \gamma_a$  and  $\alpha^l \leq \gamma_a$ .
- (ii) The radius of the parent tube element must not be smaller than the radius of the connection candidate:  $r^j \leq \gamma_r r^l$ .
- (iii) The connection distance must not be too large:  $d \leq \gamma_d r^j$ . Using radius  $r^j$  as an additional factor makes the formulation independent of the scale of the actual application domain (e.g. airways of men or animals).

To yield correct connections in case of tangential or overlapping tubular structures, a combination of distance and angle is used to compute the connection confidence for all possible connections:

$$\text{conf}(\mathbf{x}_i^j, \mathbf{x}_k^l) = e^{-\frac{d^j}{2r^j}} \frac{1}{1 + \frac{1}{r^j} d}. \quad (9)$$

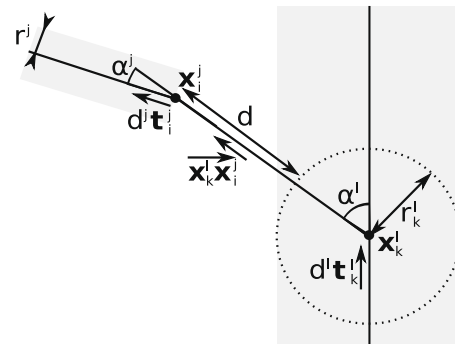


**Fig. 5.** Information used for calculation of the confidence function for tree reconstruction (Section 3.2.2).

The pair of points  $\mathbf{x}_i^l$  and  $\mathbf{x}_k^l$  with the highest connection confidence is determined and a connection path in the image domain is obtained using linear interpolation. After determining the path, the gray-values of the pixels along this path are analyzed to verify the correctness of the connection. Therefore the maximal gray value difference between the path points and the average gray value of the considered tube elements is determined:  $\text{diff} = \max_{\mathbf{x} \in \text{path}} |I(\mathbf{x}) - (\bar{I}^i + \bar{I}^k)/2|$ . A connection candidate with too large deviations  $\text{diff} > \gamma_{\text{diff}}$  is discarded as invalid and the next most plausible connection candidate is considered for reconnection. Setting this parameter to twice the standard deviation of the image noise is a good choice. Note, that this step only serves to verify the plausibility of the connection. This plausibility verification is not incorporated into the confidence function directly as verification for all possible connections would be computationally expensive.

After determination and verification of the best possible connection, the tube element is connected to the corresponding tree and the structural forest description is updated. During this step the flow direction of the newly added tube element of the tree is determined, dependent on the endpoint of the tube element that is connected.

### 3.3. Constrained segmentation

To accurately delineate the boundary of tree structures, the gathered information about structure (skeleton and estimated radius) is utilized as shape priors to guide the segmentation process (Fig. 2). The actual segmentation is constrained to an image region in proximity of the expected surface by defining object and background seed regions as shown in Fig. 6. Therefore, the information about centerline point locations  $\mathbf{x}_i^l$  and associated radii  $r_i^l$  are used to calculate the signed distance to the shape prior (tube) surface  $D_{\text{surface}}(\mathbf{x})$  and the distance to the closest centerline point  $D_{\text{centerline}}(\mathbf{x})$  using fast marching methods. Based on  $D_{\text{surface}}(\mathbf{x})$  and  $D_{\text{centerline}}(\mathbf{x})$ , the object ( $D_{\text{surface}}(\mathbf{x}) < -d_m$  or  $D_{\text{centerline}}(\mathbf{x}) < d_{\min}$ ) and background seed regions ( $D_{\text{surface}}(\mathbf{x}) > d_{om}$ ) are defined. Additionally, the signed distance  $D_{\text{surface}}(\mathbf{x})$  determines the assignment of individual pixels to different trees in case of multiple trees. This also guarantees non-overlapping segmentation results in case of partly overlapping tubular objects.

The objective of the segmentation step is to find the optimal surface that separates the object from the background seed regions. This is done by finding a closed surface  $S$  in between, whose associated energy  $E(S) = \oint_S g(\mathbf{x}) d\mathbf{x}$  is minimized. The term  $g$  with  $g \geq \epsilon > 0$  represents the costs and is based on edge information. A globally optimal solution to a discretized formulation of this minimization problem is determined using the graph cut algorithm (Boykov et al., 2001). Therefore, the voxels of an image are repre-

sented as nodes of a graph. Nodes representing adjacent voxels in the image are connected by an edge with associated costs  $g(\mathbf{x})$  (the costs are computed as the average costs of the values computed at the discrete voxels). The utilized cost term  $g(\mathbf{x})$  incorporates the gradient magnitude  $|\nabla G_\sigma \star I|$  and a soft shape prior based on  $D_{\text{surface}}$  that emphasizes edge information in proximity of the expected tube surface:

$$g(\mathbf{x}) = e^{-\frac{|\nabla G_\sigma \star I(\mathbf{x})|^2}{2\sigma_{\text{edge}}^2}} \left( 1 - \alpha e^{-\frac{D_{\text{surface}}(\mathbf{x})^2}{2\sigma_{\text{shape}}^2}} \right), \quad (10)$$

where  $0 \leq \alpha \leq 1$  can be used to control the influence of the shape prior.  $\sigma$  depends on the image noise level, while  $\sigma_{\text{edge}}$  depends on the contrast and is application specific. The value of  $\sigma_{\text{shape}}$  depends on the maximally expected variation from a perfectly tubular shape.

## 4. Evaluation and case studies

In general, the evaluation of tubular tree segmentation methods is a difficult problem due to the complex topology of tubular systems (e.g. vessel systems). Usually, reference segmentations are generated and utilized for evaluation, but with complex interwoven tree structures this is practically infeasible. To overcome this problem, our evaluation is based on three parts, each of them evaluating different aspects of our method. The first part is based on CT scans of a plastic phantom. Using a digital model of the plastic phantom as ground truth, we quantify the methods tube detection performance and segmentation accuracy under varying imaging conditions. The second part of our evaluation is based on clinical contrast enhanced liver CT datasets containing multiple interwoven vessel trees. Based on an assessment by a radiologist, we quantify the ability of our method to correctly obtain the structure of the different trees. In addition, the segmentation accuracy is evaluated based on a qualitative scoring scheme. In the third part the robustness of our method is assessed.

### 4.1. Phantom datasets

To evaluate the performance of our approach under the influence of varying noise levels, scan resolutions, contrast situations, and tube diameters, we produced a plastic phantom “vessel tree” with known digital ground truth. The design of the “vessel tree” (Fig. 7(a)), that was manufactured with a rapid prototyping machine, is inspired by the branching pattern of the human portal vein tree of the liver and consists of about 600 cylindrical branches with varying orientation and diameter (1–16 mm). The phantom was scanned with a Siemens Somatom Sensation 64 CT scanner with various resolutions to produce different noise, partial volume effects, and image reconstruction artifacts. To generate different contrast situations, different “backgrounds” were used: water and water enriched with contrast agent (Fig. 7(c) and (d)). In Table 1, estimates for the contrast (gray value difference between homogeneous regions inside the phantom and the background) and the noise level (standard deviation in a homogeneous background region) are summarized. With decreasing resolution, the noise level decreases due to the averaging effect of the larger volume of a single voxel. For some datasets, the noise level is almost as high as the contrast difference.

All CT scans of the phantom were segmented with the proposed method after adaption of the parameters on one single dataset (the high resolution dataset with water as background). The parameters used for processing of all datasets were:  $r_{\min} = 0.5$  mm,  $r_{\max} = 8.5$  mm,  $r_{\text{step}} = 1.0$  mm,  $\eta = 0.7$ ,  $t_{\text{high}} = 5.0$ ,  $t_{\text{low}} = 3.0$ ,  $t_{\text{conf}} = 300$  for the detection and extraction of tubular objects (Section 3.1),  $c_{\min} = 0.1$ ,  $\rho = 0.5$ ,  $\gamma_d = 3.0$ ,  $\gamma_a = \frac{\pi}{2}$ ,  $\gamma_r = 1.3$  for the tree

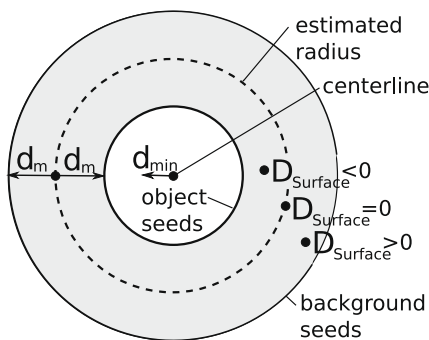
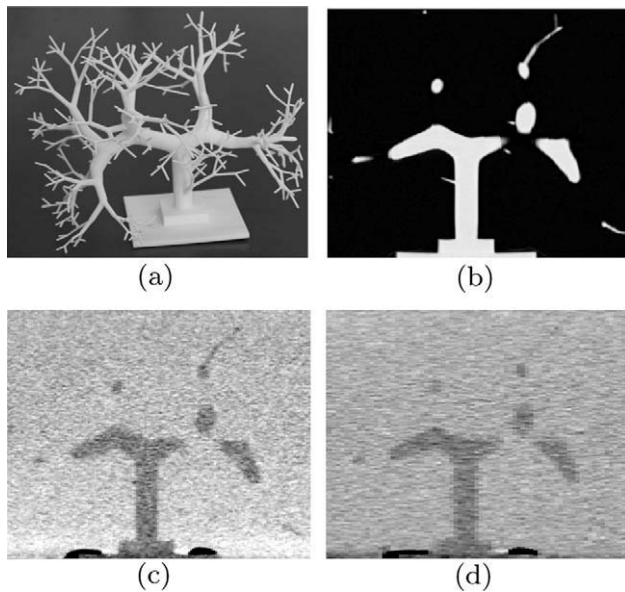


Fig. 6. Obtaining the shape prior for the constrained segmentation (Section 3.3).



**Fig. 7.** Rigid plastic “vessel” tree and image slices of the resulting phantom datasets for varying backgrounds and scanning resolutions. (a) The plastic “vessel” tree. (b) Ground truth of the phantom vessel tree shows thin branches that are not visible in some of the CT scans. (c) Background: water and contrast agent. Resolution:  $0.59 \times 0.59 \times 1.5$  mm. (d) Background: water. Resolution:  $0.59 \times 0.59 \times 3.0$  mm.

**Table 1**

Measured contrast difference between phantom and background and standard deviation of the noise for different background types and scan resolutions.

Resolution	Background			
	Water		Water and contrast agent	
	Contrast [HU]	Noise [HU]	Contrast [HU]	Noise [HU]
$0.59 \times 0.59 \times 0.5$ mm	−44.03	40.31	−55.83	39.68
$0.59 \times 0.59 \times 1.5$ mm	−43.28	17.25	−55.51	19.60
$0.59 \times 0.59 \times 3.0$ mm	−42.62	13.11	−55.57	14.77

reconstruction (Section 3.2), and  $\sigma = 2.0$ ,  $\alpha = 0.5$ ,  $d_m = 3.0$  mm,  $d_{min} = 0.5$  mm for the segmentation (Section 3.3). The remaining parameters were set to the default values listed in the methodology section.

The surfaces of the resulting segmentations were registered to the ground truth (rigid transformation) before error measures were calculated. The error measures are based on the centerline descriptions of the ground truth and on the binary segmented volumes. To establish a relationship between an arbitrary point  $\mathbf{x}$  of the segmentation and a centerline point  $\mathbf{x}_i^j$  of the known ground truth,  $\mathbf{x}$  is assigned to the point that minimizes  $\|\mathbf{x} - \mathbf{x}_i^j\|$ . This allows a correct assignment in proximity of branch points. For the computation of average errors, tubes with similar diameter were grouped together into discrete diameter bins.

#### 4.1.1. Tube detection

Based on the centerline description and the registered segmentations, tubes of the reference model were classified as detected or undetected, and the false negative rate and the false positive rate were calculated. We counted a ground truth tube as detected, if at least 80% of its centerline points have a corresponding centerline point in the result within a maximal distance of 2 mm. This formulation is necessary to tolerate inaccuracies of the centerline description that result from the not uniquely defined centerline descriptions in proximity of furcations. Fig. 8 summarizes the per-

centages of undetected tubes for the varying contrast situations, scan resolutions, and tube diameters. In all datasets, all tubes with a diameter above or equal to 3 mm were detected. As expected, the detection rate decreases with decreasing contrast and scan resolution, but even some of the very thin tubes can be detected in cases of low contrast and low inter-slice resolution. We also tested for false positive responses of the tube detection filter, but none were found.

#### 4.1.2. Segmentation accuracy

For quantification of the segmentation accuracy, the relative tube diameter error is used, because typical volume- or distance-based segmentation accuracy measures would be influenced by the remaining registration error. For computation of the tube diameter, every voxel of the final segmentation was assigned to its corresponding centerline point in the ground truth. Based on the volume of the tube elements and the lengths of the centerlines, the diameter  $d_m$  was calculated for every detected tube under the assumption of a perfect cylindrical shape. Based on  $d_m$ , the relative diameter error  $|d_m - d_k|/d_k$  was calculated, where  $d_k$  denotes the known (true) tube diameter. Fig. 9 summarizes the results for varying contrast, tube diameter, and scan resolution, averaged over all tubes with a similar diameter. As can be seen, the segmentation error decreases with increasing scan resolution. For very thin tubular objects, performance seems to be slightly better for the datasets with water as background (Fig. 9(a)). However, only very few tubes were detected (Fig. 8(a)) and consequently the resulting statistic is not very meaningful. In absolute numbers, the largest diameter error found over all datasets was 1.24 mm for a tube with a diameter of 3 mm scanned at a voxel resolution of  $0.59 \times 0.59 \times 3.0$  mm with water as background.

#### 4.2. Clinical liver datasets

A quantitative assessment of our method on CT phantom data was presented in the previous section. In this section, an evaluation of our approach on clinically acquired contrast enhanced liver CT datasets is presented. The main focus of this evaluation was to assess, if all liver vessels are detected and if the structures of the different vascular trees is correct. In addition, the vessel segmentation quality was also assessed in terms of suitability for clinical application (e.g., planning of surgery) by using a scoring scheme. Basically, the liver has three vessel systems consisting of portal veins, hepatic veins, and hepatic arteries. Depending on the used imaging protocol, different parts of the liver vasculature can be visible due to contrast enhancement.

Our method to separate multiple interwoven vessel trees has been evaluated using 15 clinical contrast CT datasets that show at least portal and hepatic veins. In 10 out of the 15 cases, livers included tumors or metastases. In one case, the right liver lobe was resected. For segmentation, the same set of parameters as on the phantom data (Section 4.1) was used on all datasets. The root elements of the different vascular trees were selected manually. This information is required for the tree reconstruction (Section 3.2) and allows the user to select the vascular systems to be segmented.

For evaluation, an expert radiologist was asked to assess the above outlined evaluation criteria. To facilitate this process, we provided the radiologist an interactive visualization system. The user interface allows to visualize the CT datasets as MIPs or cutting planes (multiplanar reconstruction). In addition, the segmentation results of the different trees can be visualized as colored skeletons, meshes, or as contour outlines displayed on the cutting plane. The user interface also allows to: interactively change the visualization by moving the cutting plane, manipulate the display gray-value range as well as transparency, display the different vessel trees individually or together, and overlay different visualizations

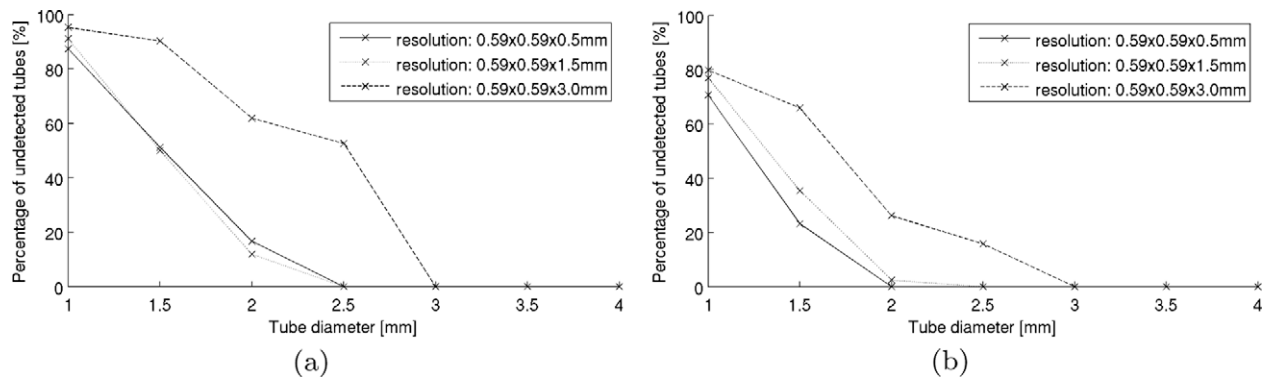


**Fig. 8.** Percentage of undetected tubes (false negatives) for varying contrast situations, scan resolutions, and tube diameters. (a) Background: water. (b) Background: water and contrast agent.

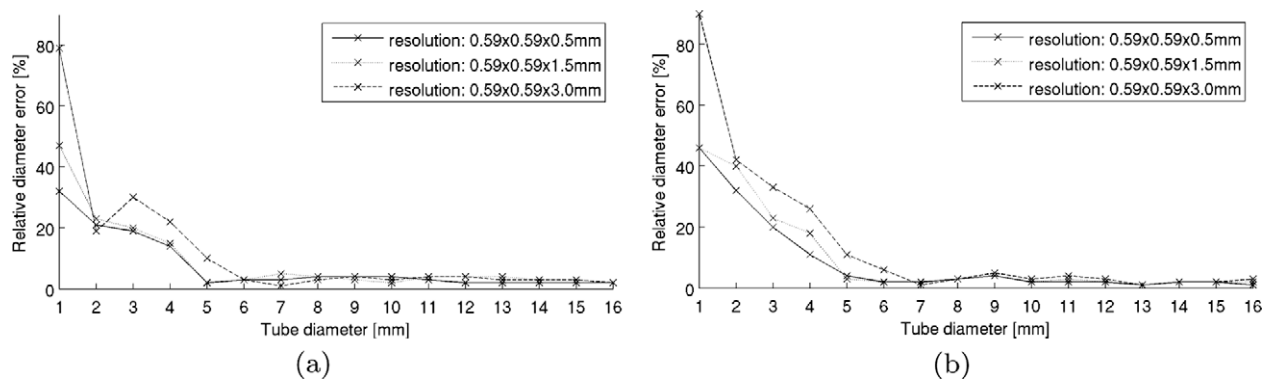


**Fig. 9.** Segmentation error (relative tube diameter error) for varying contrast situations, scan resolutions, and tube diameters. (a) Background: water. (b) Background: water and contrast agent.

among each other. Such overlays provide an effective way to judge the correctness and quality of vessel segmentations. In the following paragraphs, we present the results of this assessment (Table 2).

#### 4.2.1. Completeness/correctness of vessel branches

The radiologist was asked to identify false positive (non-existing vessel branches) or false negative (missing vessel branches) branches in the 15 segmented datasets. Note that we denote the vessel parts between bifurcations or the vessel parts at the end of the tree structures as branches. While no false positives were generated by our method, 11 (0.26%) vessel branches were identified as missing in the segmentation results (Table 2). Overall, 4159 vessel branches out of the 4170 true vessel branches were correctly identified. The majority of the missing vessel branches have a small diameter and low contrast. The largest missing vessel is shown in Fig. 10, and an example concerning the portal artery is shown in Fig. 11. Examples for the successful segmentation of poorly contrasted vessels and vessels in close proximity to a tumor are shown in Figs. 12 and 13, respectively.

#### 4.2.2. Correctness of connections/tree separation

The ability to reconstruct and simultaneously separate different interwoven vessel systems is one of the key features of our approach. For evaluation, all branch connections were assessed and judged as “correct” or “incorrect”, similar to the work of Bullitt et al. (2001). In addition, we quantified the effect of each single misconnection by counting the number of affected branches as measure for the size of the affected subtree. Out of the 4159 branches that were assessed during the evaluation, only 3 (0.072%) connections were classified as incorrect, with a total num-

ber of 8 (0.19%) affected branches. An example is shown in Fig. 14. All errors affected distal trees which consisted of up to three branches. No misconnection of larger vessels was observed.

#### 4.2.3. Data and segmentation quality

CT data quality and segmentation quality were assessed qualitatively by the radiologist, ranking them as “poor”, “ok”, or “good”. A summary of all scores is given in Table 2. For evaluation, results of several individual hepatic vessel trees of a liver were combined. Note that we have excluded results for portal arteries, because they were only visible in 3 of the 15 utilized datasets (imaging protocol). Data quality is primarily related to the noise level, scan resolution, and contrast between vessels and liver parenchyma. Note that different vascular systems can have a different score for the same dataset. The segmentation quality measure is utilized to evaluate the quality/accuracy of the identified vessel boundaries. As part of this evaluation, we took the non-uniform contrast agent distribution in different generations of the vessel systems into account. Consequently, we assessed the number of visible generations and the segmentation quality related to different vessel generations. In case of “good” data quality the segmentations were always scored as “good” in all generations, while cases with “poor” data quality and only a few visible generations, the segmentation quality tended to be scored as “ok”. This is in particular the case towards the distal parts of the portal vein tree where the contrast vanishes completely. None of the segmentations was scored as “poor”. A plot of the contrast of the main vessel trunk versus the combined centerline length for each dataset is shown in Fig. 15. As can be seen, the contrast varies considerably and has a strong influence (correlation) on the resulting centerline length.



**Table 2**

Summary of evaluation results on clinical liver CT datasets. The qualitative scores are on a scale of 1–3 with 1 = “poor”, 2 = “ok”, and 3 = “good”. The “–” sign indicates that no vessels in these generations were visible.

Dataset	# Detected branches	# Missing branches	# Mis-connections	# Affected branches	Portal vein tree			Hepatic vein tree		
					Data quality	# Visible generations	Segmentation quality in generation	Data quality	# Visible generations	Segmentation quality
							0/1 2/3 4/5			Proximal Medial Distal
d1	524	2 (0.38%)	0	0	3	4	3 3 3	3	3	3 3 3
d2	210	0	0	0	2	2	3 2 –	3	3	3 3 3
d3	162	0	0	0	3	3	3 3 –	3	3	3 3 3
d4	625	0	0	0	3	5	3 3 3	3	3	3 3 3
d5	566	0	0	0	2	5	3 3 3	1	3	2 2 2
d6	224	0	1 (0.45%)	3 (1.34%)	3	4	3 3 3	3	3	3 3 3
d7	304	0	0	0	2	3	3 2 –	1	3	3 3 3
d8	212	3 (1.40%)	0	0	2	3	3 2 –	1	3	3 3 3
d9	453	0	0	0	3	5	3 3 3	3	3	3 3 3
d10	138	0	0	0	2	4	3 3 2	1	2	3 3 –
d11	117	0	0	0	3	3	3 3 –	3	3	3 3 3
d12	102	0	2 (1.96%)	5 (4.90%)	3	3	3 3 3	3	3	3 3 3
d13	70	0	0	0	2	2	2 2 –	1	2	3 3 –
d14	380	3 (0.78%)	0	0	2	4	3 3 3	2	3	3 3 3
d15	72	3 (4.00%)	0	0	2	3	3 3 –	1	2	2 2 –
Average	277.27	0.73 (0.26%)	0.2 (0.07%)	0.53 (0.19%)						

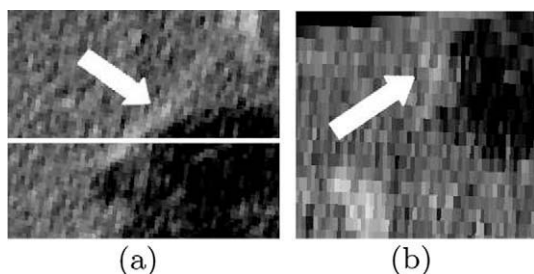


**Fig. 10.** Unsegmented vessel (arrow) found by the radiologist. (a) Axial cutting plane through the dataset. (b) Coronal cutting plane indicated by the white line in (a) shows anisotropy.

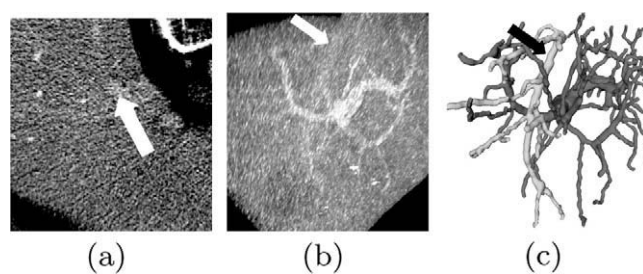


**Fig. 12.** Successful segmentation of poorly contrasted hepatic vessels (arrow). (a) Cutting plane through the dataset shows the trunk of the hepatic veins. (b) MIP of the dataset. (c) Segmentation result.

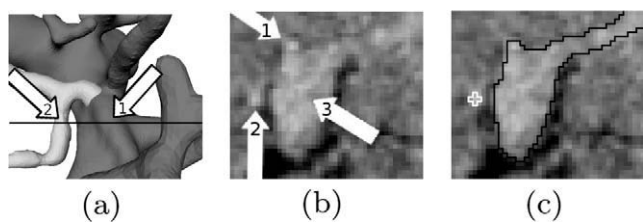


**Fig. 11.** Unsuccessfully detected portal artery. (a) Segmentation result shows the hepatic artery (bright) in proximity of the portal vein (dark). (b) Cutting plane through the dataset indicated by the black line in (a), shows two hepatic arteries (1 and 2) close to the portal vein (3). (c) While artery (2) was successfully detected, artery (1) was too close to the portal vein such that no centerline was detected/extracted. Instead, this part of the artery was segmented as part of the portal vein.

#### 4.3. Assessment of robustness

##### 4.3.1. Impact of flow direction

Contrary to other approaches, our method incorporates flow direction information for reconstruction and separation of trees from unconnected tubular objects (Section 3.2). To assess the impact of this approach on robustness, we removed all parts in our tree reconstruction step that utilizes flow direction (angle) information. We applied this simpler algorithm to five of the liver datasets utilized in Section 4.2. The selection was made based on the

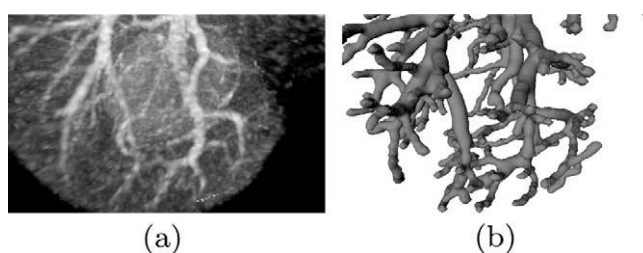


**Fig. 13.** Successful segmentation of vessels in close proximity of a bright tumor. (a) MIP of dataset. (b) Segmentation result.

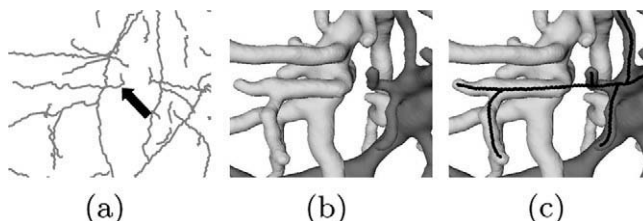


**Fig. 14.** Wrong vessel connection identified by radiologist. (a) Identified vessels; black arrow indicating vessel that was falsely connected to the wrong parent vessel. (b) Segmentation result shows falsely reconstructed vessel trees. (c) The black line indicates the correct vessel structure.

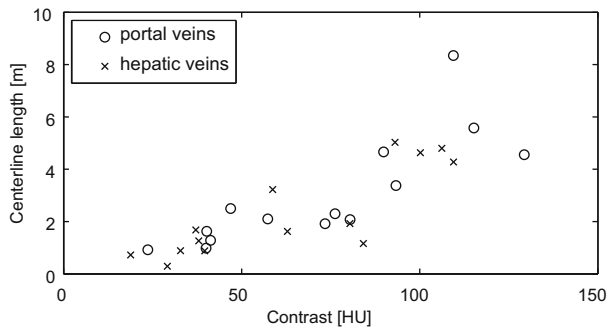


**Fig. 15.** Relation between image contrast and length of the extracted portal veins and hepatic veins of the liver.

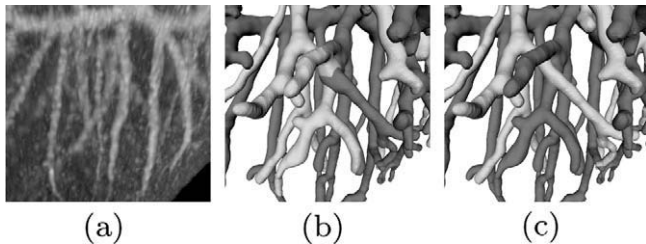


**Fig. 16.** Effect of incorporating flow direction information into the tree reconstruction and separation. (a) MIP showing two interwoven vessel systems. (b) Segmentation result without using flow direction information, showing some misconnected vessel branches. (c) Segmentation result using flow direction information, showing a successful separation.

accumulated centerline length, and the five datasets with the longest centerlines were selected. If no flow direction information was used, 23 misconnections occurred. The misconnections affected combined 98 vessel branches. The largest affected subtree consisted of 18 branches. With flow direction, only one misconnection occurred that affected three branches which corresponded to one subtree. Two examples showing errors resulting from omitting flow direction information are shown in Figs. 16 and 17. As can be seen, flow direction information enhances the robustness of our algorithm considerably.

#### 4.3.2. Abnormal tube shape

To test the robustness of our method regarding variations in tube shape, we utilized it to segment four pathological abdominal aortas in contrast enhanced CT datasets. The aortas had stenosis or

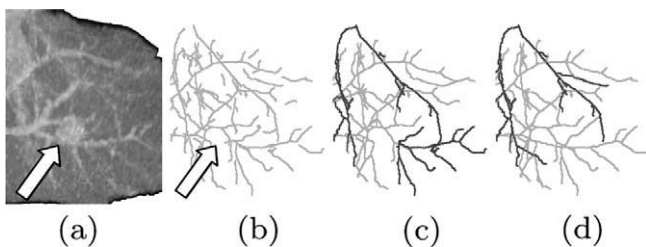


**Fig. 17.** Example of the reconstruction of the portal (bright) and hepatic (dark) vein trees from detected tube elements/centerlines. (a) MIP of the dataset using a liver mask; some vessels are only barely visible because of low contrast to the background and high image noise. (b) Extracted tube elements/centerlines before tree reconstruction; In the area adjacent to the tumor the portal veins were not detected (arrow). (c) Reconstructed trees without using flow direction information shows larger areas of the portal veins attached to the hepatic vein tree. (d) Reconstructed trees using flow direction information shows a successful reconstruction of the vessel systems including the vessel adjacent to the tumor.

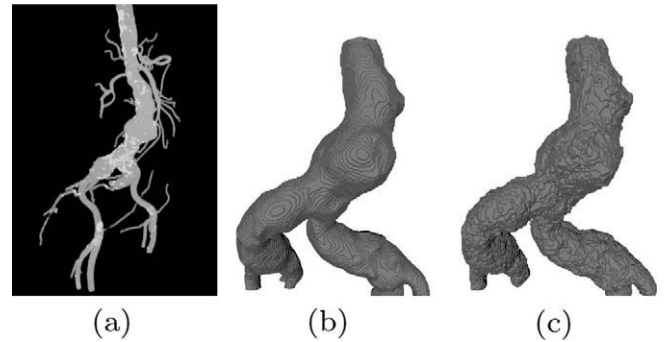


**Fig. 18.** Segmentation of an abdominal aorta tree. (a) MIP of the complete aortic tree after segmentation with the proposed method. The dataset contains larger aneurysms and calcifications. (b) Subvolume shows the segmentation result of our approach. (c) Subvolume showing the reference segmentation.

aneurysms as well as calcifications (Fig. 18(a)), thus the shape deviated significantly from a standard cylindrical tube shape. For each dataset, a semi-automatically generated reference segmentation in a subvolume around the aneurysm/stenosis was available for comparison. Segmentation results showed an average unsigned surface distance error of  $0.5 \pm 0.1$  mm, which is lower than the average intra-slice resolution of the datasets. The average unsigned volume error was  $2.1 \pm 1.8\%$ . A segmentation result is depicted in Fig. 18(b) and the corresponding reference is shown in Fig. 18(c).

## 5. Discussion

### 5.1. Performance and robustness

We have evaluated our method in Section 4 on several different datasets to assess the ability to: (a) correctly obtain/separate different tree structures (e.g., vessel systems), (b) accurately determine the surface of tubular tree structures (segmentation accuracy), and (c) robustly handle noise, disturbances (e.g., tumors), and deviation from cylindrical tube shapes (e.g., aneurysms). In this section, we discuss different aspects of the evaluation.

#### 5.1.1. Structural correctness

On experiments with phantom and clinical data, we demonstrated our method's ability to identify tubular objects (Sections 4.1 and 4.2). In all experiments, no false positives were detected, demonstrating the robustness of our method to imaging artifacts and noise. With decreasing contrast and scan resolution, the detection of thin tubular objects becomes increasingly difficult, and at some point, tubes become indistinguishable from the image background. Using phantom datasets, we quantified the effect of contrast and resolution on the detectability of tubular objects. On clinical liver CT datasets, we showed the correlation between contrast and the centerline lengths of the extracted vessel trees (Fig. 15). For clinical liver datasets, the radiologist identified only a few missing vessel branches (11 (0.26%) out of 4170). On phantom data, far more missing tubes were identified (Fig. 8). In case of the phantom datasets, the location and number of tubular branches was known a priori, because of the available ground truth. Note that most of the unidentified tubes in the phantom datasets can not be visually detected in the image data by humans (Fig. 7). Clearly, for clinical data, no such ground truth was available. Overall, our method performed well even in case of poor data quality.

We demonstrated the ability of our method to separate and segment multiple interwoven vessel trees on clinical CT datasets

(Section 4.2). As shown in our experiments, utilizing information about flow direction in the tree structures (e.g., blood flow in vessel systems) was an important factor in obtaining the correct structure of multiple overlapping (vessel) trees (Sections 4.2 and 4.3.1).

### 5.1.2. Segmentation accuracy

On phantom datasets we quantified the segmentation accuracy for tubular objects with different radius under varying imaging conditions (Section 4.1). Investigated contrasts and scan resolutions showed almost no effect on the accuracy in case of vessels with larger diameter. For thin tubular objects the statistics was not very meaningful, because only a few tube elements were detectable (about 90% undetected) due to low contrast, noise, and low resolution. For all successfully identified vessels, the absolute radius error stayed within an one voxel range (inter-slice resolution). Note that the used graph cut segmentation is only able to produce voxel accurate segmentations. We also scored the segmentation accuracy on liver CT datasets in terms of clinical usability for surgical planning (Section 4.2). The majority of segmented branches were scored as “good” and no branch was scored as “poor”, even for datasets with “poor” data quality. For low quality datasets with only few visible generations, the segmentation tended to be scored as “ok” toward the distal parts of the vessel trees where the contrast almost vanishes.

### 5.1.3. Robustness

Our method performed robustly on the clinical datasets of the liver CT data as shown in our evaluation. For example, it produced correct results in disturbed regions caused by adjacent tumors (Figs. 13 and 19). All liver datasets utilized in our evaluation contained multiple overlapping vessel trees that had to be separated, and 11 out of the 15 datasets had pathological variations where other methods are likely to fail, as discussed in Section 5.2. Our method also performed well in case of abnormal tube shapes, as our evaluation of the segmentation accuracy on abdominal aorta datasets showed (Section 4.3.2). On all phantom, clinical liver, and abdominal aorta datasets, one common set of parameters was used, although the datasets show a large variation in data quality and contrast. Only for the abdominal aorta some parameters had to be adapted to account for the much larger size.

## 5.2. Comparison to other methods

### 5.2.1. Vessel segmentation and separation

In this section, we compare our method with two different vessel segmentation approaches proposed by Selle et al. (2002) and Manniesing et al. (2006) on liver CT data (Section 4.2). The first method (Selle et al., 2002) was specifically designed for liver vessel

separation and segmentation. It is a refined top-down region growing approach combined with a method for the separation of overlapping vessel trees based on the analysis of skeletons after segmentation. Selle et al. (2002) did not present a performance evaluation, but mentioned the need to manually adapt parameters for each dataset. In addition, they utilized a tool to correct errors in the tree separation. The second method is based on level sets and was originally utilized for cerebral vessel segmentation (Manniesing et al., 2006). Both methods require a liver mask for preprocessing and the segmentation. Fig. 19(b) and (c) show segmentation results of these methods on a typical contrast enhanced liver CT dataset. Both methods utilize primarily gray-value information for segmentation. Consequently, the tumor shown in Fig. 19(a) is included in the segmentation results. Selle's approach to tree separation was able to remove major parts of the hepatic veins from the initial portal vein tree segmentation result. However, some errors still remain in the segmentation result (Fig. 19(b)). The result achieved with the algorithm of Manniesing et al. (2006) contains some parts of the hepatic vein and the tumor is connected to the portal vein tree (Fig. 19(c)). In comparison, our approach resulted in a correct segmentation shown in Fig. 19(d). Our high-level analysis step during the tree reconstruction allows to resolve problems as explained in Fig. 17, and a valid shape prior is generated such that leakage or undersegmentation is avoided. The ability to consider local disturbances in a more global context contributes to the robustness of our approach and is one of the major advantages.

### 5.2.2. Tube detection

One key factor for the robust performance of our approach is a reliable tube detection method. Our tube detection filter suppresses responses to surface patches and allows avoidance of responses between closely adjacent objects by computation of the boundary information on a smaller scale (Fig. 20(d)). A comparison to the methods of Krissian et al. (2000, 2003) is shown in Figs. 20(e) and (f), respectively. For the default case of a single tubular objects all methods perform similarly well. While the original formulation of Krissian et al. (2000) produces responses to surface patches (Fig. 20(e) on the very right), their later approach (Krissian et al., 2003) allow reduction of this effect. Both methods produce undesired responses between the closely tangential tubular objects (Figs. 20(e) and (f)).

## 5.3. Application to other domains and future work

The development of our method was motivated by the need to reliably segment the different vascular systems of the liver in order to facilitate liver surgery planning (Reitinger et al., 2006). However,

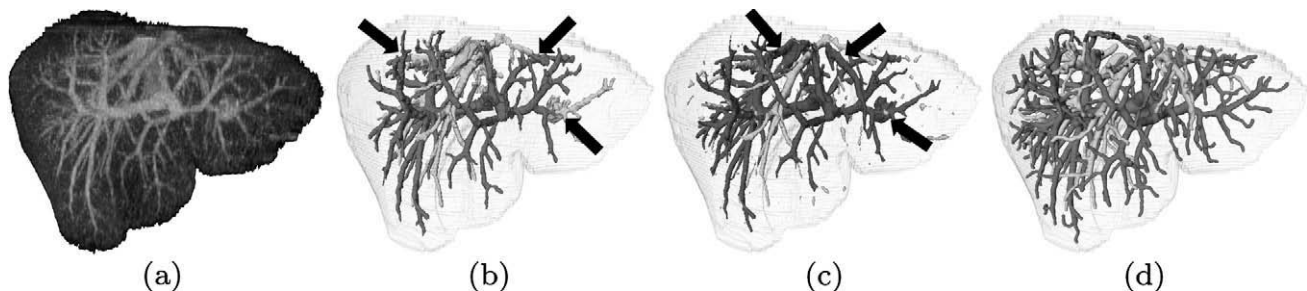


**Fig. 19.** Separation and segmentation of liver vessel trees in a contrast enhanced CT dataset (dark: portal veins, bright: remaining vessels). The dataset contains a tumor in close proximity to the portal vein tree and hepatic veins that overlap in the image with the portal vein tree due to partial volume effects. An image slice of the datasets is shown in Fig. 1(b). (a) MIP of the dataset using a liver mask. (b) Segmentation results generated with Selle's approach (Selle et al., 2002) showing erroneous portal vein and hepatic vein separation. (c) Segmentation result of the level set based method (Manniesing et al., 2006) showing isolated vessel segments and leakage of the portal vein tree into hepatic veins and the tumor. (d) Segmentation result of the proposed method.



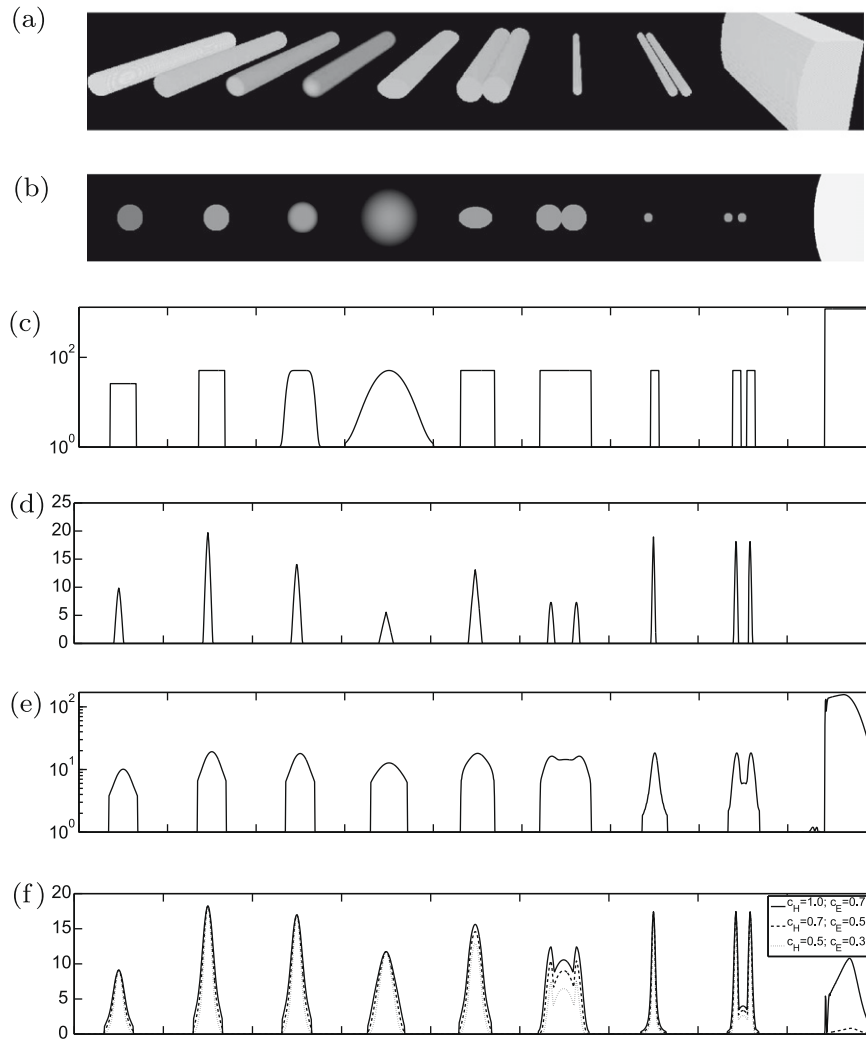


**Fig. 20.** Tubular structures with varying cross-section profile representing situations found in typical CT datasets and responses of the proposed tube detection filter and other methods with similar objectives. Note that for some plots logarithmic scales are used to capture the full value range of values. (a) 3d volume rendering. (b) 2d cross-sections. (c) 1d cross-sections. (d) Response of proposed method ( $\eta = 0.5$ ). (e) Response of Krissian et al., 2000 method with suggested parameters. (f) Response of Krissian et al., 2003 method with suggested parameters. Additionally the parameters  $c_H$  and  $c_E$  were varied (suggested:  $c_H = 1.0$ ,  $c_E = 0.7$ ).

the concepts developed are generally applicable as demonstrated in Section 4.3.2 and depicted in Fig. 21. Preliminary results achieved with the method for segmentation of lung vasculature and airway trees were promising and adaption/evaluation of our method for these tasks will be part of our future work. Further, we will investigate the development of appropriate visualization and interaction techniques for the proposed method to deal with

detected subtrees that can not be connected automatically in case of too severe disturbances. One example of such a case is shown in Fig. 21, where a tumor infiltrates and blocks one airway branch of the lung completely. The segmentation result of our approach after selecting the trachea as root of the airway tree is shown in Fig. 21(c) where the lower left airway branch is missing in the segmentation result because of conflicting gray value evidence between the airway branches. Contrary to conventional approaches, our approach enables an identification of this problem as the missing airway branch is detected. This allows a proper reaction to this situation, either by segmenting the remaining airway branch separately or by connecting the two parts of the airway tree.

## 6. Summary and conclusion

In this paper, we presented and validated an approach for simultaneous 3d separation and segmentation of multiple interwoven tubular tree structures in medical image data. In contrast to conventional approaches, our approach does not solely rely on low-level information like gray value or local shape description for segmentation. Instead, our approach initially performs an identification of tubular objects followed by a high-level analysis

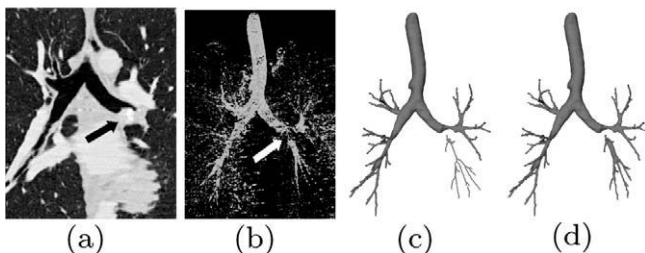


**Fig. 21.** Segmentation of an airway tree with a large tumor infiltrating the airway (arrows). (a) Coronal slice of the dataset shows the tumor. (b) Volume rendering of the dataset. (c) Segmentation after specifying a root point inside the trachea. (d) Segmentation after selecting the root of the remaining airway branch.



to obtain the structure of the different trees. This structure information is then utilized as a prior to constrain the intrinsic segmentation process. By using this strategy, problems like separation of different tubular trees/systems or handling of local disturbances are addressed on a global level by utilizing information about all identified tubular objects and the flow direction in the biological tree structures. Consequently, our approach outperforms other methods that only consider local information. We evaluated our approach on phantom and clinical datasets. Results show a high robustness of our approach against disturbances, the methods ability to successfully reconstruct, separate, and accurately segment multiple interwoven tubular tree structures. Experiments demonstrate that the proposed concept is well suited for several different application domains.

## Acknowledgments

This work was supported in part by the Austrian Science Fund (FWF) under the doctoral program Confluence of Vision and Graphics W1209 and Grants P14897-N04 and P17066-N04. The authors thank Prof. Dr.-Ing. Georgios Sakas for providing the CT datasets of the thorax.

## References

- Agam, G., Armato, S.G., Wu, C., 2005. Vessel tree reconstruction in thoracic CT scans with application to nodule detection. *IEEE Trans. Med. Image* 24 (4), 486–499.
- Aylward, S., Bullitt, E., 2002. Initialization, noise, singularities, and scale in height ridge traversal for tubular object centerline extraction. *IEEE Trans. Med. Image* 21 (2), 61–75.
- Beichel, R., Pock, T., Janko, C., Zotter, R., Reitering, B., Bornik, A., Palágyi, K., Sorantin, E., Werkgartner, G., Bischof, H., Sonka, M., 2004. Liver segment approximation in CT data for surgical resection planning. In: *Medical Imaging 2004: Image Processing*, San Diego, CA, USA, pp. 1435–1446.
- Boykov, Y., Jolly, M.-P., Jul, 2001. Interactive graph cuts for optimal boundary & region segmentation of objects in n-d images. In: *Proceedings of ICCV*, Vancouver, Canada, pp. 105–112.
- Bullitt, E., Aylward, S., Smith, K., Jukherji, S., Jiroutek, M., Muller, K., 2001. Symbolic description of intracerebral vessels segmented from magnetic resonance angiograms and evaluation by comparison with X-ray angiograms. *Med. Image Anal.* 5 (2), 157–169.
- Dou, X., Wu, X., Wahle, A., Sonka, M., 2009. Globally optimal surface segmentation using regional properties of segmented objects. In: *Proceedings of SPIE*, Lake Buena Vista, FL, USA.
- Frangi, A.F., Niessen, W.J., Vincken, K.L., Viergever, M.A., 1998. Multiscale vessel enhancement filtering. In: *Medical Image Computing and Computer-Assisted Intervention*, MICCAI, pp. 130–137.
- Frangi, A.F., Niessen, W.J., Hoogeveen, R.M., van Walsum, T., Viergever, M.A., 1999. Model-based quantitation of 3-d magnetic resonance angiography images. *IEEE Trans. Med. Image* 18 (10), 946–956.
- Kirbas, C., Quek, F., 2003. A review of vessel extraction techniques and algorithms. *IEEE Trans. Med. Image* 20 (2), 117–131.
- Krissian, K., Farneback, G., 2003. Techniques in the enhancement of 3D angiograms and their applications. In: Leondes, C.T. (Ed.), *Medical Imaging Systems Technology Methods in Cardiovascular and Brain Systems*, vol. 5. Springer, Berlin, pp. 359–396.
- Krissian, K., Malandain, G., Ayache, N., Vaillant, R., Troussset, Y., 2000. Model-based detection of tubular structures in 3D images. *Comput. Vis. Image Understand.* 2 (80), 130–171.
- Krissian, K., Ellsmere, J., Vosburgh, K., Kikinis, R., Westin, C.-F., 2003. Multiscale segmentation of the aorta in 3d ultrasound images. In: *Engineering in Medicine and Biology Society, Proceedings of the 25th Annual International Conference of the IEEE*, Cancun, Mexico, pp. 1720–1729.
- Lee, J., Beighley, P., Ritman, E., Smith, N., 2007. Automatic segmentation of 3d micro-ct coronary vascular images. *Med. Image Anal.* 11 (4), 630–647.
- Li, H., Yezzi, A., 2007. Vessels as 4-d curves: global minimal 4-d paths to extract 3-d tubular surfaces and centerlines. *IEEE Trans. Med. Image* 26 (9), 1213–1223.
- Lorigo, L., Faugeras, O., Grimson, W., Kerivenc, R., Kikinis, R., Nabavid, A., Westin, C., 2001. Curves: curve evolution for vessel segmentation. *Med. Image Anal.* 5 (3), 195–206.
- Manniesing, R., Velthuis, B., van Leeuwen, M., van der Schaaf, I., van Laar, P., Niessen, W., 2006. Level set based cerebral vasculature segmentation and diameter quantification in CT angiography. *Med. Image Anal.* 10 (2), 200–214.
- Pock, T., Janko, C., Beichel, R., Bischof, H., 2005. Multiscale medialness for robust segmentation of 3D tubular structures. In: *Computer Vision Winter Workshop*, pp. 93–102.
- Reitering, B., Bornik, A., Beichel, R., Schmalstieg, D., 2006. Liver surgery planning using virtual reality. *IEEE Comput. Graph. Appl.* 26 (6), 36–47.
- Risser, L., Plouaboue, F., Descombes, X., 2008. Gap filling of 3-d microvasculature networks by tensor voting. *IEEE Trans. Med. Image* 27 (5), 674–687.
- Sato, Y., Nakajima, S., Shiraga, N., Atsumi, H., Yoshida, S., Koller, T., Gerig, G., Kikinis, R., 1998. Three-dimensional multi-scale line filter for segmentation and visualization of curvilinear structures in medical images. *Med. Image Anal.* 2 (2), 143–168.
- Selle, D., Preim, B., Peitgen, H., 2002. Analysis of vasculature for liver surgical planning. *IEEE Trans. Med. Image* 21 (11), 1344–1357.
- Soler, L., Delingette, H., Malandain, G., Montagnat, J., Ayache, N., Koehl, C., Dourthe, O., Malassagne, B., Smith, M., Mutter, D., Marescaux, J., 2001. Fully automatic anatomical, pathological, and functional segmentation from CT scans for hepatic surgery. *Computer Aided Surg.* 6 (3), 131–142.
- Steger, C., 1998. An unbiased detector of curvilinear structures. *IEEE Trans. Pattern Anal. Mach. Intell.* 20 (2), 113–125.
- Szymczak, A., Stillman, A., Tannenbaum, A., Mischaikow, K., 2006. Coronary vessel trees from 3d imagery: a topological approach. *Med. Image Anal.* 10 (4), 548–559.
- Wink, O., Niessen, W., Viergever, M., 2004. Multiscale vessel tracking. *IEEE Trans. Med. Image* 23 (1), 130–133.
- Xu, M., Pycock, D., 1999. A scale-space medialness transform based on boundary concordance voting. *J. Math. Image Vis.* 11 (13), 277–299.
- Yi, J., Ra, J.B., 2003. A locally adaptive region growing algorithm for vascular segmentation. *Int. J. Imaging Syst. Technol.* 13 (4), 208–215.